





<https://doi.org/10.1038/s42005-023-01134-y>

OPEN

Evolution of anisotropic magnetic properties through helix-to-fan transition in helical antiferromagnetic EuCo_2As_2

Jong Hyuk Kim¹, Mi Kyung Kim ^{1✉}, Jae Min Hong¹, Hyun Jun Shin ¹, Ki Won Jeong¹, Jin Seok Kim¹, Kyungsun Moon¹, Nara Lee ^{1✉} & Young Jai Choi ^{1✉}

A helimagnet comprises a noncollinear spin structure formed by competing exchange interactions. Recent advances in antiferromagnet-based functionalities have broadened the scope of target materials to include noncollinear antiferromagnets. However, a microscopic understanding of the magnetic anisotropy associated with the intricate evolution of noncollinear spin states has not yet been accomplished. Here, we have explored the anisotropic magnetic aspects in a layered helimagnet of EuCo_2As_2 by measuring the magnetic field and angle dependence of the magnetic torque. By adopting an easy-plane anisotropic spin model, we can visualize the detailed spin configurations that evolve in the presence of rotating magnetic fields. This is directly related to the two distinctive magnetic phases characterized by the reversal of the magnetic torque variation across the helix-to-fan transition. Our advanced approach provides an in-depth understanding of the anisotropic properties of noncollinear-type antiferromagnets and a useful guidance for potential applications in spin-processing functionalities.

¹Department of Physics, Yonsei University, Seoul 03722, Korea. ✉email: kkummi.mi@yonsei.ac.kr; eland@yonsei.ac.kr; phylove@yonsei.ac.kr

The identification of material parameters that crucially influence intrinsic magnetic properties is a key element in finding suitable materials for magnetic functionalities. Magnetocrystalline anisotropy is of particular significance for stabilizing the preferred orientation of spin configurations and dominating the evolution of anisotropic magnetic features under magnetic fields^{1–3}. It emerges from the anisotropic nature of spin–orbit interactions and varies depending on the structure and symmetry of the magnetic compounds^{4,5}. Following the establishment of the perception that antiferromagnetic (AFM) order governs dynamic magnetotransport, the field of antiferromagnetic spintronics has rapidly developed, thus providing innovative concepts to realize spin-processing device applications^{6–15}. However, collinear antiferromagnets are generally exploited as the basic element for spintronic functionalities. In this regard, detailed examinations of anisotropic characteristics in noncollinear antiferromagnets can expand the scope of the target materials and construct generic foundations to manipulate anisotropy for extensive magnetic applications.

EuCo_2As_2 (ECA) belongs to the ThCr_2Si_2 -type structure family and crystallizes in a body-centered tetragonal structure (I4/mmm space group) with lattice constants of $a = 0.391$ nm and $c = 1.153$ nm (See Supplementary Note 1)^{16,17}. In such layered compounds, the two- or three-dimensional nature arises with respect to the interlayer bonding strength, and the physical properties can be controlled by chemical doping^{17,18}. This results in a variety of electronic and magnetic states, such as the heavy fermion behavior in CeCu_2Si_2 ^{19,20}, Fe-based superconductivity in K-doped BaFe_2As_2 ^{21,22}, and intricate magnetic phase diagrams based on unconventional magnetism in $(\text{La,Nd})\text{Co}_2\text{P}_2$ ²³. ECA has a two-dimensional characteristic, which allows it to be mechanically exfoliated. The magnetic Eu^{2+} ions ($S = 7/2$ and $L = 0$) show a helimagnetic order with slight incommensurability of the propagation vector $\mathbf{k} = (0, 0, 0.79)$, as confirmed by a previous neutron diffraction experiment¹⁷. In contrast, the magnetic moments of Co ions are paramagnetic, irrespective of the temperature^{16,24}.

Helimagnets have a prototypical noncollinear spin structure, in which the spin direction is rotated spatially in the plane, but the rotation axis is parallel to the propagation direction²⁵. The zero net moment associated with rotating spins in a helimagnet shares the advantages of collinear-type antiferromagnets, such as the absence of a stray field and ultrafast spin dynamics^{26–30}. However, the study of magnetic anisotropy in noncollinear antiferromagnets remains to be explored because of the difficulty in analyzing the complicated spin states formed during the application and rotation of the magnetic field. In this study, we performed a detailed investigation of the magnetic anisotropy in helimagnetic EuCo_2As_2 by exploiting the magnetic torque measurements. The magnetic field along the axis perpendicular to the helical axis results in a helix-to-fan magnetic transition, across which the angle-dependent torque is progressively reversed. The microscopic spin model with planar magnetocrystalline anisotropy allows the verification of the continuously varying spin states formed during the rotation of the magnetic fields, which would be challenging to be determined from scattering experiments due to the limiting field geometry. Further, we quantified the strength of exchange couplings and magnetocrystalline anisotropy, and correlated the estimated spin states directly with the reversal trend in angle-dependent torque data through the helix-to-fan transition. It is distinctive from most ordinary inferences on the magnetic torque data, drawn by the simple fitting use of a series of sinusoidal functions deduced by the angle derivative of the magnetic free energy^{31–34}.

Results

Structure and magnetic properties. The crystallographic and spin structures are depicted in Fig. 1a, b. Two Co_2As_2 layers are placed opposite to each other and are separated by a magnetic Eu layer. The net magnetic moment in the Eu layer rotates in the ab plane with propagation along the c -axis. In Fig. 1b, viewed from the c -axis, five different Eu spins stacked along the c -axis are shown to overlap in each Eu. The angle between the two Eu moments for the adjacent layers is 142.2° , which indicates that the pitch of the helix is slightly incommensurate. The schematics in Fig. 1c show the helix structure that is formed in zero magnetic field (H) and fan structure in H along the a axis. The AFM interaction between the nearest Eu layers with the comparable AFM interaction between the next-nearest Eu layers lead to the helical order in ECA, which emerges at $T_N = 46$ K. The magnetic susceptibility, $\chi = M/H$, where M is the magnetization, was measured at $H = 1$ T upon warming after zero- H -cooling for the a - (χ_a) and c - (χ_c) axes, as shown in Fig. 1d, e, respectively. The anomaly at the Néel temperature, T_N verifies the onset of the helical AFM order, and the large inclination of χ_a is compatible with the spins favorably oriented in the ab plane.

In a collinear antiferromagnet, a sufficient strength of H along the magnetic easy axis may induce a spin-flop or spin-flip transition, determined by the relative strength of the magnetocrystalline anisotropy^{35–37}. Through the magnetic transition, the AFM phase converts to a flopped or flipped phase, along with distinct anomalies of magnetic properties. Such an anomalous feature can also be found in noncollinear-type antiferromagnets. As shown in Fig. 2a, a sudden increase in M_a (M along the a -axis) appears at $H_m = 4.7$ T and $T = 2$ K and indicates a helix-to-fan transition^{16,27,38,39}. The fan phase can be characterized by the net magnetic moments oscillating spatially along the propagation vector. A behavior similar to the spin-flop transition is presented by the extrapolation of the linear slope above H_m merging at the origin. A slight magnetic hysteresis, as shown in the inset of Fig. 2a, manifests the first-order nature of this transition⁴⁰. Owing to the strong magnetic anisotropy, M_c (M along the c -axis) increases linearly, which is ascribed to the continual canting of the net moments. While the slope of M_c is constant, the slope of M_a , which is smaller than that of M_c below H_m , becomes larger across H_m .

Easy-plane anisotropic spin model. A substantial aspect of the helix-to-fan structure was examined theoretically by introducing an easy-plane anisotropic spin model (see “Methods” in detail). We considered the commensurate helical spin structure ($k = 0.8$) for the convenience of calculation. The competing exchange energy for the relative angle φ of the two adjacent moments is given by $E/N = 2S^2(J_1\cos\varphi + J_2\cos 2\varphi)$, where J_1 and J_2 represent the AFM coupling strengths between the Eu^{2+} moments of the two nearest and next-nearest layers, respectively, and $S = 7/2$ for the Eu^{2+} ions. Energy minimization yields $\varphi = \cos^{-1}(-\frac{J_1}{4J_2})$ and $J_2 = 0.31J_1$ at $\varphi = \frac{4}{5}\pi$ for the helical order in the ECA³⁸. By tracing the minimum total magnetic energy in the presence of H for the full spin Hamiltonian, we theoretically calculated M_a and M_c as a function of H . By fitting the theoretical result of M_a to the experimental data taken at 2 K, we obtained the following relations using $H_m = 4.7$ T: $g\mu_B H_m/J_1 S = 1.18$, $K_5 = 0.022J_1 S$, and $J_2^2 = 5.45 \times 10^6 \text{ Jm}^{-3}$, where the electron g-factor $g = 2$ and μ_B denotes the Bohr magneton⁴¹. Fitting the theoretical result of M_c to the experimental data that were taken at 2 K leads to the additional relation $K_\theta = 0.35J_1 S^2 = 1.96 \times 10^6 \text{ Jm}^{-3}$, consistent with the previous work⁴¹. The calculated M_a and M_c , as plotted in Fig. 2b, d, agree well with the measured data upon including the magnetocrystalline anisotropy in the ac plane. The absence of a

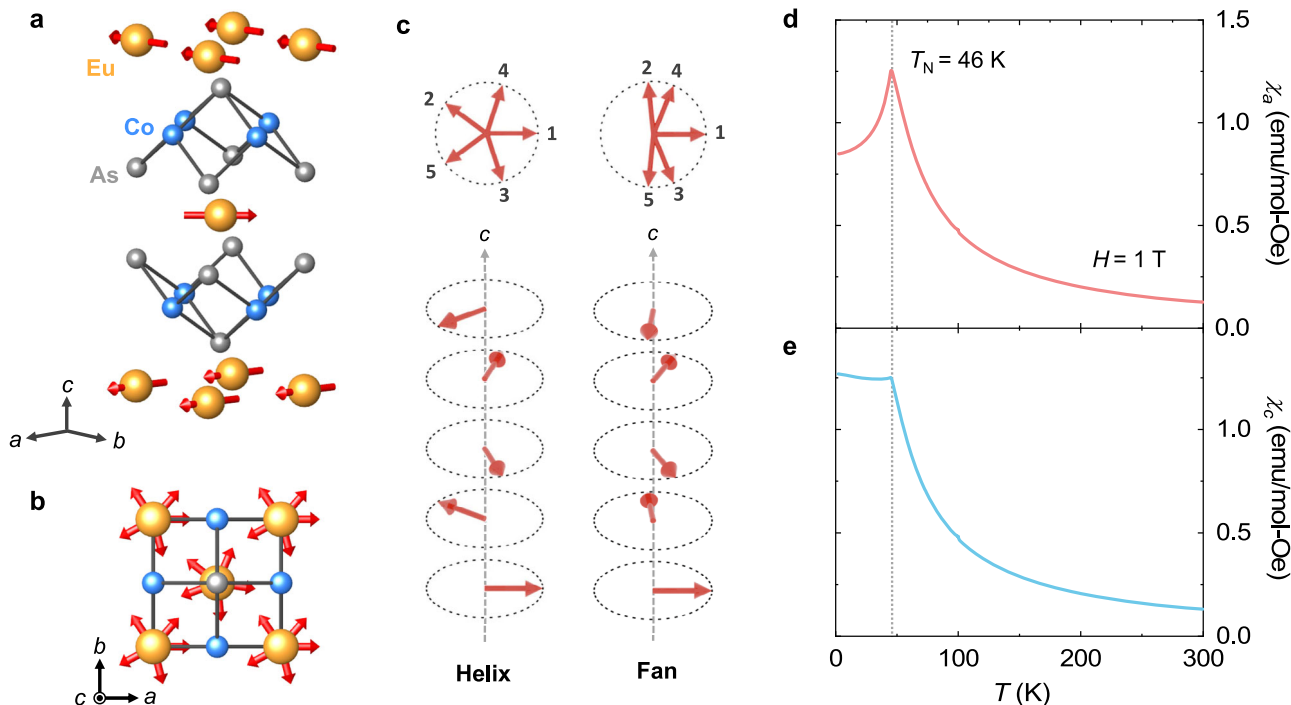


Fig. 1 Structure and magnetic susceptibility. **a** Side view of the crystallographic and magnetic structures of EuCo_2As_2 (ECA). The orange, blue, and grey spheres denote Eu, Co, and As atoms, respectively. The red arrow on each Eu indicates the individual spin direction. The net Eu moment in a layer rotates spatially in the ab plane with the propagation vector $\mathbf{k} = (0, 0, 0.79)$. **b** Top view of the crystal and magnetic structures. Five different spins stacked along the c -axis are shown overlapped in each Eu. **c** Schematics of helical ($k = 0.8$) and fan structures, respectively. In the schematics, all arrows corresponding to the net magnetic moments in each Eu layer begin from a single common point in the center. The Eu layers are numbered from 1 to 5 around the c -axis. **d** Temperature (T)-dependent magnetic susceptibility $\chi = M/H$, measured upon warming at $H = 1$ T after zero-field cooling for the a -axis, χ_a . The vertical gray line denotes the Néel temperature, $T_N = 46$ K. **e** T -dependent χ for the c -axis, χ_c , taken at $H = 1$ T after zero-field cooling.

four-fold rotational anisotropy in the ab plane, which can be ascribed to the tetragonal structure, indicates that the helical spin order forms independently of the ab planar crystalline axes. The merit of our model calculation is evident in the direct quantification of the spin configurations formed during the shift from the helix to the fan state, as illustrated in Supplementary Fig. 1 and listed in Supplementary Table 2 (Supplementary Note 2). The orientations of the net moments in the helical state ($H_a = 4$ T) turn considerably in the H_a direction, as illustrated Fig. 2b. In the fan state, the moments away from the H_a direction tend to be close together perpendicularly and convert further to the H_a direction under a strong $H_a = 9$ T (Fig. 2b). In contrast, for the hard spin c -axis, the net moments are continually canted in the direction of H_c , which leads to the formation of a chiral conical state, as shown in the inset of Fig. 2d.

The magnetocrystalline anisotropy in ECA tends to restrict the orientations of the net moments within the ab plane, and competing AFM interactions result in a stable helical phase at zero H ¹⁷. H_a triggers phase conversion to the fan phase with considerable variation in M_a . As T is increased, H_m lowers slightly till 20 K, but decreases faster above 20 K (Fig. 3a). H_m at 40 K was observed to be 2.9 T, determined by the derivative of M_a . The anomalous feature at H_m also diminishes with increasing T . The slope of M_a after H_m is attributed to the additional canting of the net moments in the fan state, whose behavior is maintained up to a higher T . The linearly increasing trend of M_c remains intact at a higher T , which exhibits a gradual canting of the net moments to the rotation axis (Fig. 3b). At 40 K, a slight decrease in the slope above 7 T is observed in both M_a and M_c , which reflects the influence of thermal fluctuations interfering with the additional canting of the net moments to the field direction (Fig. 3a, b).

Anisotropic magnetic-torque properties. The anisotropic magnetic properties and occurrence of the helix-to-fan transition can also be investigated by performing an experiment on the magnetic torque per unit volume, $\tau = \mathbf{M} \times \mathbf{H}$, as plotted in Fig. 3c, d^{31,42–46}. For the rotation of H in the ac plane, ϑ is the angle of H deviating from the c -axis, as shown in the schematic (inset of Fig. 3d) ($\vartheta = 0^\circ$ for the c -axis and $\vartheta = 90^\circ$ for the a -axis). At ϑ slightly smaller than 90° , magnetic torque (τ) starts from zero and increases positively as H is increased, reaching a peak at H_m . After H_m , τ gradually decreases and changes to negative values by crossing zero at ~ 6.7 T. A larger deviation from 90° generates an improved peak at H_m . As ϑ becomes larger than 90° , τ is entirely reversed because the relative angle between M and H changes its sign at 90° . However, at ϑ near 0° , small and broad variations were observed by sweeping H . The difference in the behavior of τ indicates the largely anisotropic nature of the ECA crystals.

The development of anisotropic magnetic properties across the helix-to-fan transition was examined based on the angular dependence of the magnetic τ , as shown in Fig. 4a, b^{31,42–46}. At $H = 4$ T below H_m , the slopes of τ at $\vartheta = 90^\circ$ and 270° are larger than those at $\vartheta = 0^\circ$ and 180° , which indicates the susceptible variation of τ near $\vartheta = 90^\circ$ and 270° (Fig. 4a). This anisotropic behavior is consistent with the different slopes between M_a and M_c below H_m (Fig. 2a, c). Above H_m , the anisotropic nature is adjusted by the enhanced M_a through the spin-reorientation transition, and the larger slope of M_a comparable to that of M_c (Fig. 2a, c). At $H = 7$ T, the values of τ near $\vartheta = 90^\circ$ and 270° are partly reversed, but the positive slope of τ near $\vartheta = 0^\circ$ and 180° is sustained (Fig. 4a). The sign of τ is completely reversed at $H = 9$ T because the helix-to-fan transition can be induced by a small rotation of H near $\vartheta = 0^\circ$ and 180° . The contour plots in Fig. 4b show a distinct aspect of the gradual H -driven reversal of τ above H_m . As T is

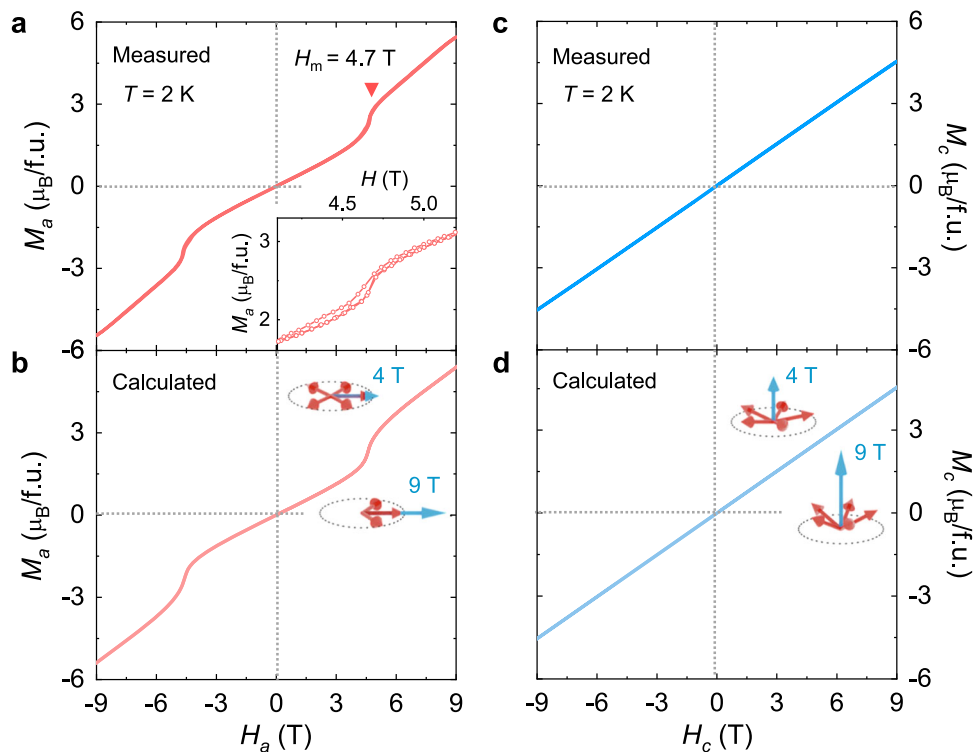


Fig. 2 Measured and calculated anisotropic magnetization. **a** Isothermal magnetization, measured along the a -axis (M_a) at $T = 2$ K. Red inverted triangle specifies the occurrence of the helix-to-fan transition, $H_m = 4.7$ T. The inset displays a magnified view of M_a , indicating the manifestation of weak magnetic hysteresis. **b** Isothermal magnetization obtained from the easy-plane spin model by fitting to the experimental M_a at $T = 2$ K. The schematics in the inset depict helical and fan states at $H = 4$ and 9 T, respectively, along the a -axis. The right blue arrow designates the magnitude and direction of H . Beginnings of the red arrows in layers indicating net magnetic moments are placed together at one point. **c** Isothermal magnetization, measured along the c -axis (M_c) at $T = 2$ K. **d** Isothermal magnetization obtained from the easy-plane spin model by fitting to the experimental M_c at $T = 2$ K. The schematics in the inset display chiral conical states at $H = 4$ and 9 T along the c -axis.

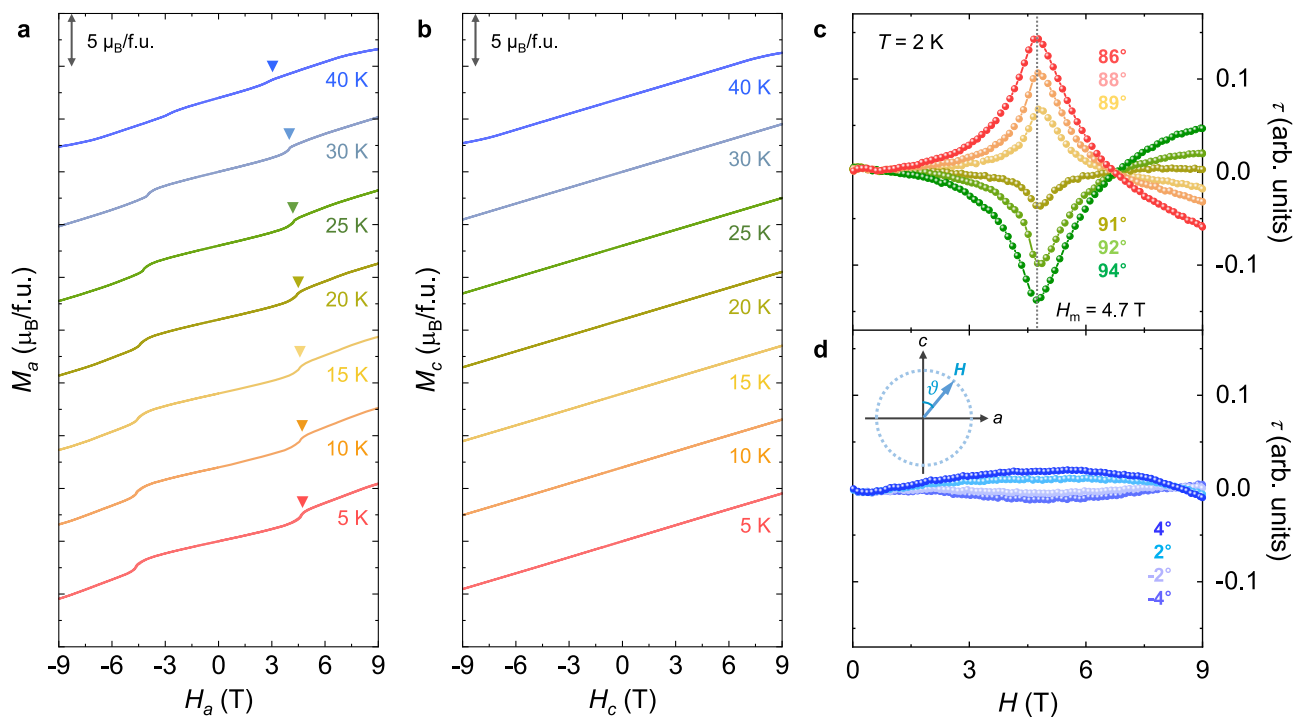


Fig. 3 Temperature evolution of anisotropic magnetization and magnetic-field-dependent torques. **a** Isothermal M_a measured at various temperatures, $T = 5, 10, 15, 20, 25, 30,$ and 40 K. The M_a data are shifted vertically for clear visualization. A marked scale indicates $1 \mu_B/f.u.$, where f.u. denotes the formula unit. The inverted triangles represent the occurrence of H_m at each T . **b** Isothermal M_c measured at various temperatures, $T = 5, 10, 15, 20, 25, 30,$ and 40 K. **c** Magnetic-field dependence of the magnetic torque, τ , measured at $\vartheta = 86^\circ, 88^\circ, 89^\circ, 91^\circ, 92^\circ,$ and 94° for $T = 2$ K. **d** H -dependent τ , measured at $\vartheta = -4^\circ, -2^\circ, 2^\circ,$ and 4° for $T = 2$ K. The inset shows the geometry of the applied H in the ac plane. $\vartheta = 0^\circ$ for the c -axis and $\vartheta = 90^\circ$ for the a -axis.

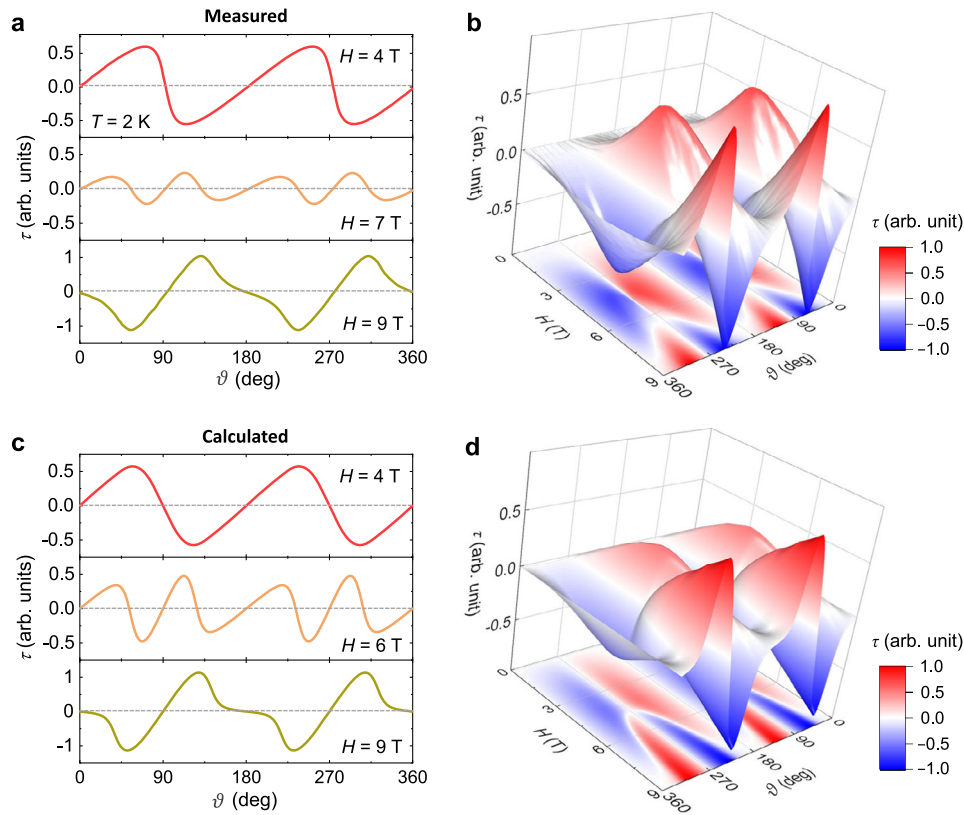


Fig. 4 Measured and calculated magnetic torques. **a** Angle dependence of magnetic torque per unit volume, $\tau = \mathbf{M} \times \mathbf{H}$, measured at $T = 2$ K by rotating H in the ac plane at $H = 4, 7$, and 9 T. $\vartheta = 0^\circ$ for the c -axis and $\vartheta = 90^\circ$ for the a -axis. The scale of τ at 9 T is two times larger than those at 4 and 7 T. **b** 3D contour plot of the angle-dependent τ data measured at different H and $T = 2$ K. A colour that corresponds to the scale of colour bar indicates the value of magnetic torque. **c** Angle dependence of τ calculated from the easy-plane anisotropic spin model at $H = 4, 6$, and 9 T. **d** 3D contour plot constructed by the angle-dependent τ data estimated at different H . A colour that corresponds to the scale of colour bar indicates the value of magnetic torque.

increased, the angle dependences are similar to the reduced values of τ and lowered H_m , as demonstrated in the plots of τ for $T = 20$ and 40 K in Supplementary Fig. 2 (Supplementary Note 3).

The angular dependence of τ was also theoretically estimated, as shown in Fig. 4c, d. By rotating a specific H , the minimum magnetic energy associated with the model Hamiltonian was calculated, generating the value of τ corresponding to the orientation of the magnetic moment in each layer at a given angle. A similar trend of τ variations as in the experiment is observed as H is increased, which indicates that the progress of the anisotropic properties through the magnetic transition can be adequately explained by the presence of easy-plane magnetocrystalline anisotropy (Fig. 4c). The contour plots of the calculated angular dependence of τ are also comparable to the experimental results (Fig. 4d). In the theoretical estimation, the partially reversed behavior of τ near $\vartheta = 90^\circ$ and 270° arises immediately after H_m because the H_a component near $\vartheta = 90^\circ$ and 270° is sufficient to trigger the helix-to-fan transition. However, in practice, the fractional reversal of τ occurs at H values higher than H_m (Fig. 4b). This can be attributed to the historical dependence of typical magnetic measurements⁴⁷. For comparison, the occurrence of the magnetic phase transition at H_m is elucidated using the H_a -dependent τ data, as shown in Fig. 3c.

Correlation between spin states and magnetic torques. In addition, the easy-plane spin model is used to establish precise net-moment configurations during the rotation of H , which manifests an intimate relationship between the diverse spin states and magnetic τ data. The value of τ is zero at $\vartheta = 0^\circ, 90^\circ$, and 180°

because of the parallel alignment between the net M and H . At $H = 4$ T, starting from $\vartheta = 0^\circ$, at which the net moment in each layer is slightly canted in the H direction, the τ value increases by the rotation of H (Fig. 5a). The net M is rotated less than H (Fig. 5b), which is compatible with the smaller slope of M_a compared with that of M_c below H_m . The deviation between the net M and H causes a positive τ and is maximized at approximately $\vartheta = 60^\circ$. With H close to $\vartheta = 90^\circ$, the net moments tend to move appreciably in the H direction. Further rotation of H over $\vartheta = 90^\circ$ induces a smooth sign change in τ with the net M rotating faster than H . τ is minimized around $\vartheta = 120^\circ$ with the maximum deviation between the net M and H and approaches zero as ϑ gets closer to 180° . Similar sign variations are obtained by fully rotating H . At $H = 6$ T, after the helix-to-fan transition, the partially reversed behavior of τ near $\vartheta = 90^\circ$ can be properly interpreted by the detailed arrangements of the net moments and angles of the net M , as shown in Fig. 5c, d. For ϑ up to approximately 60° , the positive value of τ is maintained when H is insufficient to produce the magnetic transition along the a -axis. Further rotation of H across $\vartheta = 60^\circ$ activates the transition with the orientations of magnetic moments turning considerably toward the a -axis and transforms the τ state from positive to negative by orienting the net M more than H . Across $\vartheta = 90^\circ$, another sign change occurs with the net M rotating less than H . The negative c component shows antisymmetric behavior with respect to $\vartheta = 90^\circ$. At $H = 9$ T, the overall angular dependence of τ is completely reversed, with an enhanced magnitude of τ (Fig. 5e). At a low ϑ , the net M tends to follow the direction of H , resulting in plateau-like behavior (Fig. 5f). For further rotation of H , the faster rotation of net M engenders a negative value of τ

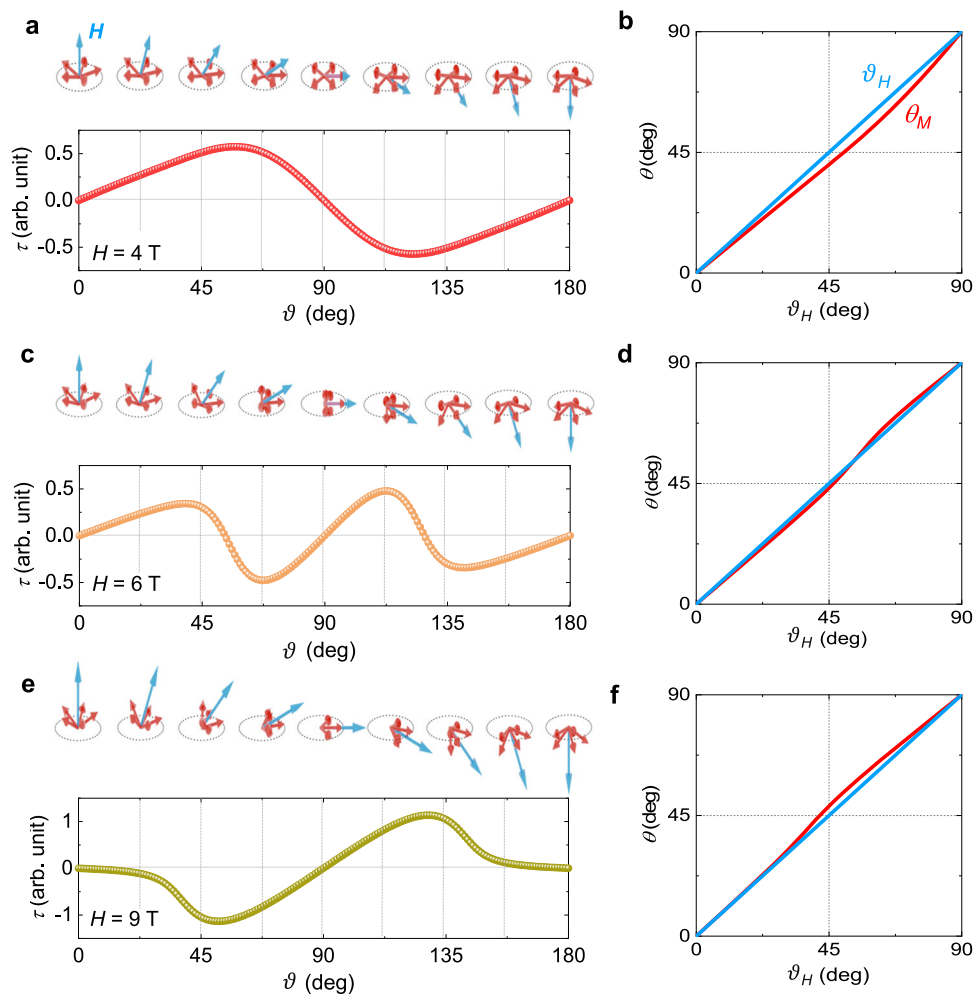


Fig. 5 Detailed magnetic-moment configurations of the angular-dependent magnetic torques. **a** Angular dependence of τ , calculated from the model Hamiltonian. H is rotated in the ac plane at $H = 4$ T. The schematics indicate the configurations of the net magnetic moments with respect to the H directions. **b** Angles of net magnetization (θ_M) with respect to the rotation of H (ϑ_H) at $H = 4$ T. **c** Calculated angular dependence of τ at $H = 6$ T. **d** θ_M with respect to ϑ_H at $H = 6$ T. **e** Calculated angular dependence of τ at $H = 9$ T. **f** θ_M with respect to ϑ_H at $H = 9$ T.

because of the magnetocrystalline anisotropy under which the spins are preferentially directed to the magnetic easy ab plane. At $\vartheta > 90^\circ$, H , which contains a negative c component, causes the net moments to turn slower than H and generates a positive τ value. The precise angles of Eu moments, attained from the easy-plane spin model, are listed in Supplementary Tables 3–5 (Supplementary Note 4).

Discussion

Magnetic torque measurement is specifically suitable for determining the angular dependence of magnetic properties with extreme sensitivity to detecting tiny torque variations. In an antiferromagnet with a certain axial or planar anisotropy, the magnetic torque is derived from the relative angle deviation between the spin- and magnetic-field directions, which is strongly affected by the magnetocrystalline anisotropy. However, most ordinary interpretations were made by the phenomenological fitting using a series of sinusoidal functions attained from the angle derivative of the magnetic free energy^{31–34}. Thus, the strength of the magnetocrystalline anisotropy and relevant spin states could not be quantified. It is also challenging to consider the magnetic phase transitions⁴⁴. In the helical antiferromagnet EuCo_2As_2 , we determined the magnetocrystalline anisotropy energy and ascertained two different magnetic phases characterized by the progressive reversal of angle-dependent magnetic

torque through the magnetic phase transition. Neutron diffraction and resonant X-ray scattering techniques used in large facilities have been generally utilized to reveal the temperature and magnetic-field evolutions of microscopic magnetic structures for noncollinear antiferromagnets^{39,48–50}. However, it is technically difficult to detect continually varying spin states in the presence of rotating magnetic fields. An obvious merit of our theoretical model calculations is the easy access to the magnetic-moment orientations in each layer by estimating the minimum magnetic energy with respect to the easy-plane anisotropic spin Hamiltonian. Our approach enables us to establish a direct connection between the spin states and magnetic torque data, and thus, provides information with regards to analysis of anisotropic magnetic properties, which can be extended to other collinear and noncollinear antiferromagnetic materials.

Methods

Sample preparation. We grew EuCo_2As_2 single crystals using the flux method with Sn flux¹⁶. A mixture of Eu, Co, As, and Sn in a 1.05:2.2:15 molar ratio was placed in a crucible vacuum-sealed in a quartz tube. The tube was kept at 1050 °C for 20 h, slowly cooled to 600 °C at a rate of 3.75 °C h^{−1}, and then cooled to room temperature at a rate of 100 °C h^{−1} in a tube furnace. Crystals with typical dimensions of 1.5 × 1.5 × 0.1 mm³ were obtained.

Magnetization and magnetic torque measurements. The temperature and magnetic-field dependences of the magnetization measurements were performed

with the field along the a - and c -axes using a vibrating sample magnetometer module in a physical property measurement system (PPMS, Quantum Design, Inc.). The magnetic torque was measured using the torque magnetometer option of the PPMS. A clean piece of the crystal was mounted on the piezoresistive cantilever of a torque magnetometer chip (P109A, Quantum Design, Inc.). With the chip on a single-axis rotator, the angle-dependent torque can be probed via a polar angle scan of the magnetic field in the ac plane. A tiny variation in torque ($1 \times 10^{-9} \text{ N} \cdot \text{m}$) can be sensitively detected by a Wheatstone bridge circuit.

Theoretical calculations. To describe the helical spin order in EuCo_2As_2 , we employ the easy-plane anisotropic spin Hamiltonian:

$$\begin{aligned} \mathcal{H}/N = & J_1 \sum_{i=1}^5 \vec{S}_i \cdot \vec{S}_{i+1} + J_2 \sum_{i=1}^5 \vec{S}_i \cdot \vec{S}_{i+2} - g\mu_B \vec{H} \cdot \sum_{i=1}^5 \vec{S}_i + K_\theta \sum_{i=1}^5 \cos^2 \theta_i \\ & - K_S S (\sin \vartheta)^4 \sum_{i=1}^5 \cos 5\varphi_i, \end{aligned} \quad (1)$$

where N denotes the number of Eu^{2+} moments in a single layer^{38,41}. We consider the helical spin structure of ECA as commensurate ($k=0.8$) for convenience of calculation, and therefore include only five layers with periodic boundary conditions. The first and second terms designate the competing exchange interactions forming a helimagnetic state, in which J_1 and J_2 denote the antiferromagnetic coupling strengths between the Eu^{2+} moments of the two nearest and next-nearest layers, respectively, and $S=7/2$ for the Eu^{2+} ions. The third term indicates the Zeeman energy. The fourth term reflects the planar magnetocrystalline anisotropy, in which the spins tend to align in the ab plane and K_θ is the magnetocrystalline anisotropy constant. Explanations of the cases involving the higher-order term of magnetocrystalline anisotropy and the impact of the number of spin layers on M_c are included in Supplementary Note 5. In the fifth term, the ferromagnetic interaction in the Eu^{2+} layer is treated as the mean field. Here, θ_i and φ_i denote the polar and azimuthal angles of the individual spin \vec{S}_i in each layer, respectively; θ_i is the angle deviating from the c axis; and φ_i is the angle rotating in the ab plane ($\varphi_i=0$ for the a axis and $\pi/2$ for the b axis). Because the planar spin rotation symmetry is explicitly broken by applying H along the a axis in the easy plane, which is taken to be the x axis, the order parameter of the helical state can be expressed as $\sum_{i=1}^5 \cos 5\varphi_i/5$. A detailed explanation regarding the mean-field term is described in Supplementary Note 5.

Data availability

The data supporting the findings of this study are available from the corresponding authors upon reasonable request. The dataset associated with the crystallographic structure that is analyzed in this study is available in the Crystallography Open Database (COD) repository, #3000404.

Received: 14 May 2022; Accepted: 13 January 2023;

Published online: 27 January 2023

References

- Blundell, S. *Magnetism in condensed matter* (Oxford University Press, 2003).
- Getzlaff, M. *Fundamentals of magnetism* (Springer Science & Business Media, 2007).
- Spaldin, N. A. *Magnetic materials: fundamentals and applications* (Cambridge University Press, 2010).
- Daalderop, G. H. O., Kelly, P. J. & Schuurmans, M. F. H. First-principles calculation of the magnetocrystalline anisotropy energy of iron, cobalt, and nickel. *Phys. Rev. B* **41**, 11919–11937 (1990).
- Darby, M. & Isaac, E. Magnetocrystalline anisotropy of ferro- and ferrimagnetics. *IEEE Trans. Magn.* **10**, 259–304 (1974).
- Baltz, V. et al. Antiferromagnetic spintronics. *Rev. Mod. Phys.* **90**, 015005 (2018).
- Jungwirth, T. et al. The multiple directions of antiferromagnetic spintronics. *Nat. Phys.* **14**, 200–203 (2018).
- Jungfleisch, M. B., Zhang, W. & Hoffmann, A. Perspectives of antiferromagnetic spintronics. *Phys. Lett. A* **382**, 865–871 (2018).
- Godinho, J. et al. Electrically induced and detected Néel vector reversal in a collinear antiferromagnet. *Nat. Commun.* **9**, 4686 (2018).
- Jungwirth, T., Marti, X., Wadley, P. & Wunderlich, J. Antiferromagnetic spintronics. *Nat. Nanotechnol.* **11**, 231–241 (2016).
- Wadley, P. et al. Tetragonal phase of epitaxial room-temperature antiferromagnet CuMnAs . *Nat. Commun.* **4**, 2322 (2013).
- Liu, Z. Q. et al. Electrical switching of the topological anomalous hall effect in a non-collinear antiferromagnet above room temperature. *Nat. Electron.* **1**, 172–177 (2018).

- Železný, J., Zhang, Y., Felser, C. & Yan, B. Spin-polarized current in noncollinear antiferromagnets. *Phys. Rev. Lett.* **119**, 187204 (2017).
- Nan, T. et al. Controlling spin current polarization through non-collinear antiferromagnetism. *Nat. Commun.* **11**, 4671 (2020).
- Gomonay, E. V. & Loktev, V. M. Spintronics of antiferromagnetic systems (review article). *Low. Temp. Phys.* **40**, 17–35 (2014).
- Sangeetha, N. S. et al. Enhanced moments of Eu in single crystals of the metallic helical antiferromagnet $\text{EuCo}_{2-x}\text{As}_2$. *Phys. Rev. B* **97**, 144403 (2018).
- Tan, X. et al. A transition from localized to strongly correlated electron behavior and mixed valence driven by physical or chemical pressure in ACo_2As_2 ($A = \text{Eu}$ and Ca). *J. Am. Chem. Soc.* **138**, 2724–2731 (2016).
- Ying, J. J. et al. Metamagnetic transition in $\text{Ca}_{1-x}\text{Sr}_x\text{Co}_2\text{As}_2$ ($x=0$ and 0.1) single crystals. *Phys. Rev. B* **85**, 214414 (2012).
- Steglich, F. et al. Superconductivity in the presence of strong Pauli Paramagnetism: CeCu_2Si_2 . *Phys. Rev. Lett.* **43**, 1892–1896 (1979).
- Li, Y. et al. Gap symmetry of the heavy fermion superconductor CeCu_2Si_2 at ambient pressure. *Phys. Rev. Lett.* **120**, 217001 (2018).
- Paglione, J. & Greene, R. L. High-temperature superconductivity in iron-based materials. *Nat. Phys.* **6**, 645–658 (2010).
- Rotter, M., Tegel, M. & Johrendt, D. Superconductivity at 38 K in the iron arsenide $(\text{Ba}_{1-x}\text{K}_x)\text{Fe}_2\text{As}_2$. *Phys. Rev. Lett.* **101**, 107006 (2008).
- Thompson, C. M. et al. Unconventional magnetism in ThCr_2Si_2 -type phosphides, $\text{La}_{1-x}\text{Nd}_x\text{Co}_2\text{P}_2$. *J. Mater. Chem. C* **2**, 7561–7569 (2014).
- Ding, Q. P., Higa, N., Sangeetha, N. S., Johnston, D. C. & Furukawa, Y. NMR determination of an incommensurate helical antiferromagnetic structure in EuCo_2As_2 . *Phys. Rev. B* **95**, 184404 (2017).
- Uchida, M., Onose, Y., Matsui, Y. & Tokura, Y. Real-space observation of helical spin order. *Science* **311**, 359–361 (2006).
- Olejnik, K. et al. Terahertz electrical writing speed in antiferromagnetic memory. *Sci. Adv.* **4**, eaar3566 (2018).
- Takeuchi, Y. et al. Chiral-spin rotation of non-collinear antiferromagnet by spin-orbit torque. *Nat. Mater.* **20**, 1364–1370 (2021).
- Yamane, Y., Gomonay, O. & Sinova, J. Dynamics of noncollinear antiferromagnetic textures driven by spin current injection. *Phys. Rev. B* **100**, 054415 (2019).
- Gurung, G., Shao, D.-F. & Tsymbal, E. Y. Spin-torque switching of noncollinear antiferromagnetic antiperovskites. *Phys. Rev. B* **101**, 140405 (2020).
- Zhao, H. C. et al. Large ultrafast-modulated Voigt effect in noncollinear antiferromagnet Mn_3Sn . *Nat. Commun.* **12**, 5266 (2021).
- Peng, Y. et al. Magnetic structure and metamagnetic transitions in the van der Waals Antiferromagnet CrPS_4 . *Adv. Mater.* **32**, 2001200 (2020).
- Modic, K. A. et al. Robust spin correlations at high magnetic fields in the harmonic honeycomb iridates. *Nat. Commun.* **8**, 180 (2017).
- Riedl, K., Li, Y., Winter, S. M. & Valentí, R. Sawtooth Torque in anisotropic $j_{\text{eff}}=1/2$ magnets: application to $\alpha\text{-RuCl}_3$. *Phys. Rev. Lett.* **122**, 197202 (2019).
- Li, M., Rousochatzakis, I. & Perkins, N. B. Reentrant incommensurate order and anomalous magnetic torque in the Kitaev magnet $\beta\text{-Li}_2\text{IrO}_3$. *Phys. Rev. Res.* **2**, 033328 (2020).
- Nagamaya, T., Yosida, K., & Kubo, R. Antiferromagnetism. *Adv. Phys.* **4**, 1–112 (1955).
- Gorter, C. J. Observations on antiferromagnetic $\text{CuCl}_2 \cdot 2\text{H}_2\text{O}$ Crystals. *Rev. Mod. Phys.* **25**, 332–337 (1953).
- Berkowitz, A. E. & Takano, K. Exchange anisotropy — a review. *J. Magn. Magn. Mater.* **200**, 552–570 (1999).
- Johnston, D. C. Magnetic structure and magnetization of helical antiferromagnets in high magnetic fields perpendicular to the helix axis at zero temperature. *Phys. Rev. B* **96**, 104405 (2017).
- Ghimire, N. J. et al. Competing magnetic phases and fluctuation-driven scalar spin chirality in the kagome metal YMn_6Sn_6 . *Sci. Adv.* **6**, eabe2680 (2020).
- Bogdanov, A. N., Zhuravlev, A. V. & Rößler, U. K. Spin-flop transition in uniaxial antiferromagnets: magnetic phases, reorientation effects, and multidomain states. *Phys. Rev. B* **75**, 094425 (2007).
- Kim, J. H. et al. Sign-tunable anisotropic magnetization and electrically detectable dual magnetic phases in a helical antiferromagnet. *NPG Asia Mater.* **14**, 67 (2022).
- Modic, K. A. et al. Resonant torsion magnetometry in anisotropic quantum materials. *Nat. Commun.* **9**, 3975 (2018).
- Perfetti, M. et al. Magnetic anisotropy switch: easy axis to easy plane conversion and vice versa. *Adv. Funct. Mater.* **28**, 1801846 (2018).
- Das, S. D. et al. Magnetic anisotropy of the alkali iridate Na_2IrO_3 at high magnetic fields: evidence for strong ferromagnetic Kitaev correlations. *Phys. Rev. B* **99**, 081101 (2019).
- Nauman, M. et al. Complete mapping of magnetic anisotropy for prototype Ising van der Waals FePS_3 . *2D Mater.* **8**, 035011 (2021).
- Yu, A. B. et al. Probing superconducting anisotropy of single crystal $\text{KCa}_2\text{Fe}_4\text{As}_4\text{F}_2$ by magnetic torque measurements. *Phys. Rev. B* **100**, 144505 (2019).
- Bauer, A., Garst, M. & Pflüderer, C. History dependence of the magnetic properties of single-crystal $\text{Fe}_{1-x}\text{Co}_x\text{Si}$. *Phys. Rev. B* **93**, 235144 (2016).

48. Scagnoli, V. et al. Induced noncollinear magnetic order of Nd^{3+} in NdNiO_3 observed by resonant soft x-ray diffraction. *Phys. Rev. B* **77**, 115138 (2008).
49. Cooley, J. A. et al. Evolution of noncollinear magnetism in magnetocaloric MnPtGa . *Phys. Rev. Mater.* **4**, 044405 (2020).
50. Chauleau, J. Y. et al. Electric and antiferromagnetic chiral textures at multiferroic domain walls. *Nat. Mater.* **19**, 386–390 (2020).

Acknowledgements

This work was supported by the National Research Foundation of Korea (N.R.F.) through grants 2016R1D1A1B01013756, NRF-2017R1A5A1014862 (SRC program: vdWMRC center), NRF-2021R1A2C1006375, and NRF-2022R1A2C1006740.

Author contributions

N.L. and Y.J.C. initiated and supervised the project. J.H.K. and J.M.H. synthesized the single crystals. J.H.K., J.M.H., H.J.S., K.W.J., and J.S.K. performed measurements of the physical properties. M.K.K. and K.M. performed the theoretical calculations. J.H.K., M.K.K., K.M., N.L., and Y.J.C. analyzed the data and prepared the manuscript. All authors have read and approved the final version of the manuscript.

Competing interests

The authors declare no competing interests.

Additional information

Supplementary information The online version contains supplementary material available at <https://doi.org/10.1038/s42005-023-01134-y>.

Correspondence and requests for materials should be addressed to Mi Kyung Kim, Nara Lee or Young Jai Choi.

Peer review information *Communications Physics* thanks Li Yin and the other, anonymous, reviewer(s) for their contribution to the peer review of this work. Peer reviewer reports are available.

Reprints and permission information is available at <http://www.nature.com/reprints>

Publisher's note Springer Nature remains neutral with regard to jurisdictional claims in published maps and institutional affiliations.



Open Access This article is licensed under a Creative Commons Attribution 4.0 International License, which permits use, sharing, adaptation, distribution and reproduction in any medium or format, as long as you give appropriate credit to the original author(s) and the source, provide a link to the Creative Commons license, and indicate if changes were made. The images or other third party material in this article are included in the article's Creative Commons license, unless indicated otherwise in a credit line to the material. If material is not included in the article's Creative Commons license and your intended use is not permitted by statutory regulation or exceeds the permitted use, you will need to obtain permission directly from the copyright holder. To view a copy of this license, visit <http://creativecommons.org/licenses/by/4.0/>.

© The Author(s) 2023